COMMUNICATION

Check for updates

Caged gold nanostars: a novel plasmonic nanoplatform with potential theranostic applications†

Aidan J. Canning [a,b] and Tuan Vo-Dinh *[a,b,c]

Here, we first introduce caged gold nanostars (C-GNS), a novel hybrid nanoplatform combining the exceptional plasmonic properties of nanostars with the loading capability of hollow-shell structures. We present two synthetic routes used to produce C-GNS particles and highlight the benefits of the galvanic replacement-free approach. FEM simulations explore the enhanced plasmonic properties of this novel nanoparticle morphology. Finally, in a proof-of-concept study, we successfully demonstrate *in vivo* hyperspectral imaging and photothermal treatment of tumors in a mouse model with the C-GNS nanoplatform.

Introduction

There has been great interest in developing different plasmonic nanostructures exhibiting optical properties that are most useful in various applications ranging from biomarker and small molecule detection to multimodal cancer therapies.[1–10] For over three decades, our laboratory has developed a wide variety of plasmonic nanoplatforms and integrated them into applications ranging from chemical sensing to biomonitoring.[10–13] One nanoparticle morphology proven to have great utility in biomedical diagnostic and treatment applications is the surfactant-free gold nanostar (GNS).[14] Previously, we first introduced a method to synthesize gold nanostars with high aspect ratio branches without toxic ionic surfactants. This biocompatible GNS platform has led to successful photothermal immunotherapy treatments in animal models.[15] Building upon the surfactant-free GNS framework, our group

subsequently introduced and refined the synthesis of bimetallic nanostars (BNS).[16] With BNS, a silver layer is deposited onto the exposed core of the GNS while the branch tips remain exposed. This silver layer shifts the plasmonic resonance of the particles from the NIR to the visible region, enabling their use in label-free surface-enhanced Raman spectroscopy (SERS) sensing and detection applications.[17] BNS particles have provided exceptional SERS enhancement for amplification-free detection of circulating miRNA biomarkers when integrated with surface-bound oligonucleotide probes.[18]

In this work, we present a unique plasmonically active structure designated, caged gold nanostars (C-GNS) for the first time. This novel nanostructure integrates a hollow shell structure for SERS reporter encapsulation and the optically tunable properties of the nanostar-based particles. To achieve this, we devised a synthesis wherein the silver layer of BNS particles acts as scaffolding for the deposition of gold in a galvanic replacement-free reaction and is subsequently removed *via* hydrogen peroxide etching. We then characterize the elemental makeup of C-GNS particles and highlight the advantages of this method over traditional galvanic replacement reactions. Further, we demonstrate and verify the loading ability of C-GNS particles with a SERS reporter. Finite Element Method (FEM) theoretical simulations indicate that a toroidal zone of intense local electromagnetic field enhancement is produced at all intersections of the nanostar branches and the inner shell wall. A photothermal analysis of the C-GNS platform resulted in impressive photothermal conversion efficiency and stability findings. Finally, in a proof-of-concept investigation into potential theranostic applications, we demonstrate *in vivo* hyperspectral imaging of reporter-loaded C-GNS particles and their performance as photothermal transducers in treating solid tumors in a murine model.

aDepartment of Biomedical Engineering, Duke University, Durham, NC 27708, USA. E-mail: tuan.vodinh@duke.edu
bFitzpatrick Institute for Photonics, Duke University, Durham, NC 27708, USA
*cDepartment of Chemistry, Duke University, Durham, NC 27708, USA*

†Electronic supplementary information (ESI) available: All methods, GNS and unsealed C-GNS COMSOL models, ICP-MS results, cytotoxicity data, sealed C-GNS characterization, additional SERS reporter encapsulation study, brightfield image of phantom, photothermal heating curve and photothermal stability study, CEM43 °C equation. See DOI: https://doi.org/10.1039/d3nr04130a

Results and discussion

The scheme in Fig. 1A illustrates the synthesis used to produce C-GNS particles. GNS were synthesized using the surfactant-
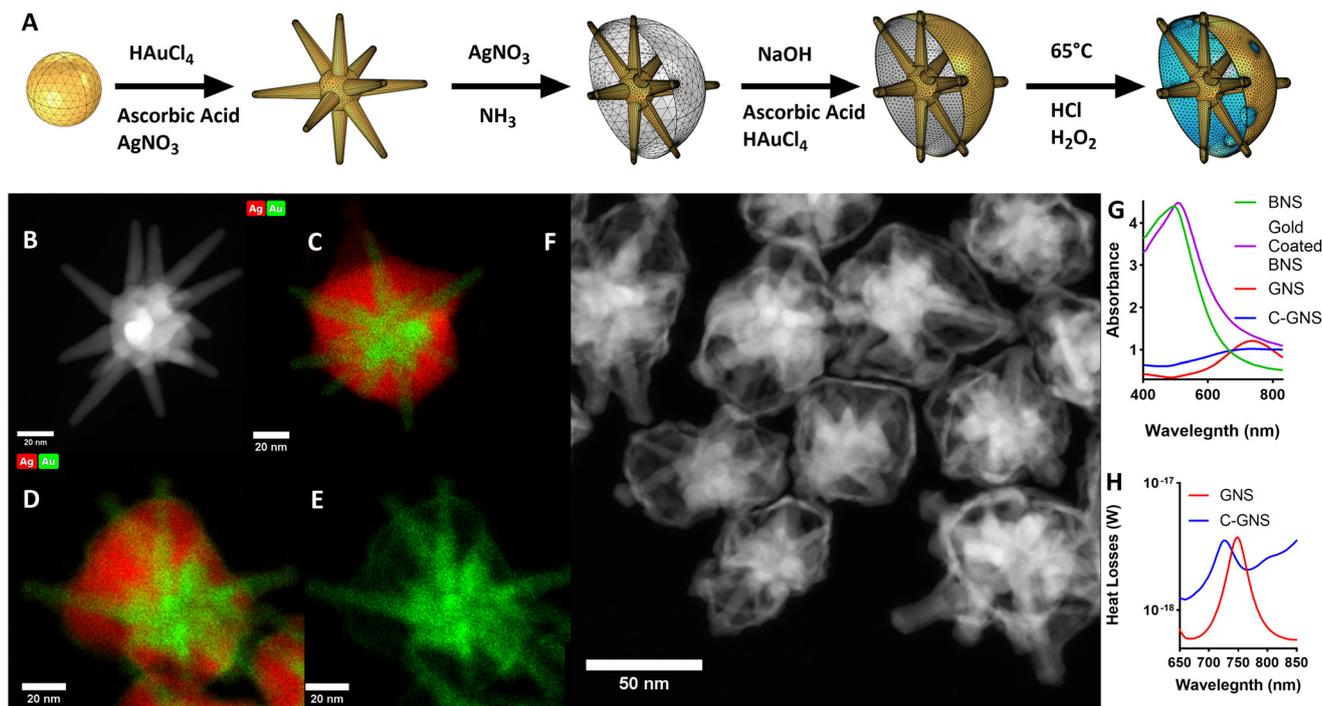
Fig. 1 Synthesis and characterization of C-GNS. (A) Scheme depicting C-GNS synthesis. (B) HAADF-STEM of GNS. (C) STEM-EDS of BNS. (D) STEM-EDS of gold-coated BNS, gold and silver overlay. (E) STEM-EDS of gold-coated BNS, gold only. (F) HAADF-STEM of C-GNS. (G) Absorption spectra of nanoparticle solutions. (H) Heat losses spectra of simulated GNS and C-GNS models.

free method previously described.[14] There, silver nitrate and ascorbic acid are added rapidly to an acidic, dilute solution of gold chloride containing 12 nm gold spheres to seed GNS branch growth. Fig. 1B depicts a representative high-angle annular dark field scanning transmission electron microscopy (HAADF-STEM) image of a typical GNS used as an initial building block of a C-GNS particle. A layer of silver was then deposited onto the exposed core of the GNS, growing outwards to the branch tips, resulting in a BNS. Fig. 1C depicts a scanning transmission electron microscopy – energy dispersive X-ray spectroscopy (STEM-EDS) image showing the overlay of the distribution of silver and gold throughout a representative BNS particle. Adapting the galvanic replacement-free deposition method developed by Yang *et al.*, BNS particles were dispersed into a basic polyvinylpyrrolidone (PVP) solution containing 0.1 M ascorbic acid.[19] Gold chloride was then added *via* a syringe pump to the solution. Fig. 1D and E show STEM-EDS images of the elemental overlay and the gold-only channel from a gold-coated BNS particle. Under these experimental conditions, the rate of gold ion reduction onto the surface of the BNS is greater than that of galvanic replacement.

Gold-coated BNS particles were washed and redispersed into an acidic 3% hydrogen peroxide solution at 65 °C to etch the golden outer shell and remove the internal silver layer. This method of hollow shell formation uses the original silver shell as a removable scaffold upon which to build the golden outer shell. This etching process results in unsealed C-GNS. Fig. 1F shows the HAADF-STEM image of several C-GNS par-

ticles after peroxide etching. The plot in Fig. 1G contains the absorption spectra of each nanoparticle solution. The plasmon resonance of GNS can be tuned in the NIR region by controlling particle branch length and aspect ratio.[20] The maximum absorbance for the representative batch shown here occurs at 736 nm. The addition of silver onto the surface of the GNS results in a dramatic blue shift of the absorbance spectrum, resulting in a peak at 498 nm. A small red-shift in peak absorbance to 513 nm is consistent with the observations made by Yang *et al.* following the completion of galvanic replacement-free gold deposition.[19] After silver oxidation and removal *via* hydrogen peroxide etching, the absorbance of the galvanic replacement-free C-GNS particle solution dramatically red shifts. This results in a peak absorbance again at 732 nm. There is a noticeable widening in the NIR of the absorption spectra between GNS and C-GNS solutions, characteristic of the formation of thin-walled plasmonic structures.[21,22] We used the wave optics module of COMSOL Multiphysics 6.0 to evaluate the structural cause of this widening, with corresponding models for GNS and C-GNS particles shown in ESI Fig. S1A and S1B.† The C-GNS model uses the same base particle as the GNS model, adding a 1 nm thick gold shell and all exposed branches with an increased radius of 1 nm. Fig. 1H contains the heat losses spectra for both particle models. This value is the result of integrating the resistive losses at each wavelength with the model volume. While the heat losses and absorption spectra describe different physical phenomena, heat losses spectra have been shown to provide information about trends

seen in absorbance spectra.[23] The difference in the absorption spectra between GNS and C-GNS particles is mirrored in the simulated heat loss spectra. The model of the GNS has a distinct peak in the mid-700s and sharply falls, whereas the C-GNS model displays a lower magnitude that is slightly blue-shifted due to branch tip widening. Also, the simulated C-GNS spectra remains high in the NIR compared to the GNS spectra, again consistent with hollow gold nano frames and other thin-walled plasmonic structures.[21,22]

Photothermal therapy leverages the high NIR absorption of nanostar-based particles to generate a local temperature increase sufficient to trigger cell death.[15,24,25] For clinical applications, particles with the highest NIR absorption are preferred as they generate heat more efficiently, reducing the minimum effective dose required. Furthermore, NIR light within the 'biological window' can travel further in tissue to reach deep tumors. Traditionally, the peak absorbance of GNS is redshifted by increasing the nanoparticle branch length and aspect ratio. However, the enhanced permeability and retention (EPR) effect, which allows for the passive targeting and accumulation of nanoparticles within the tumor microenvironment, significantly diminishes as the particle diameter increases over 125 nm.[26] Therefore, as an alternative to increasing nanoparticle size, we present the formation of C-GNS, which have increased absorption in the NIR due to the interaction between the branches and thin gold shell compared to GNS of the same size.

To confirm the advantage of preparing C-GNS particles *via* a galvanic replacement-free approach, thus significantly

decreasing the amount of gold–silver alloy that would otherwise be present in the particle shell, we also prepared a C-GNS batch through a galvanic replacement reaction. Fig. 2A and B show HAADF-STEM and STEM-EDS images of a C-GNS particle prepared through galvanic replacement. Fig. 2C and D HAADF-STEM and STEM-EDS images for a particle prepared *via* the galvanic replacement-free method. The white arrow highlights the elemental analysis region of interest in each STEM-EDS image. The intensity of silver and gold detected for each particle as a function of distance from the particle center is shown in Fig. 2B and D. When prepared using galvanic replacement, the initial shell around the nanostar core is comprised of a 1 : 2.4 gold–silver alloy. When C-GNS particles are prepared *via* the galvanic replacement-free method, the shell is comprised of a 1 : 0.32 gold–silver alloy. Also, the location of the highest silver intensity is further from the particle core compared to that of the gold within the galvanic replacement-free particle shell, suggesting that this residual silver was re-deposited on the shell rather than incorporated. Inductively coupled plasma-mass spectrometry (ICP-MS) was used to determine the elemental makeup of the sample. The results are shown in Fig. S2A,† where the gold-to-silver ratio of C-GNS particles prepared *via* galvanic replacement was 1 : 0.96 *versus* 1 : 0.14 for particles prepared using the galvanic replacement-free method. As a further contrast of the two synthetic routes capable of yielding C-GNS particles, the absorption spectra of both reactions are compared following varying amounts of gold addition as shown in Fig. 2G and H.
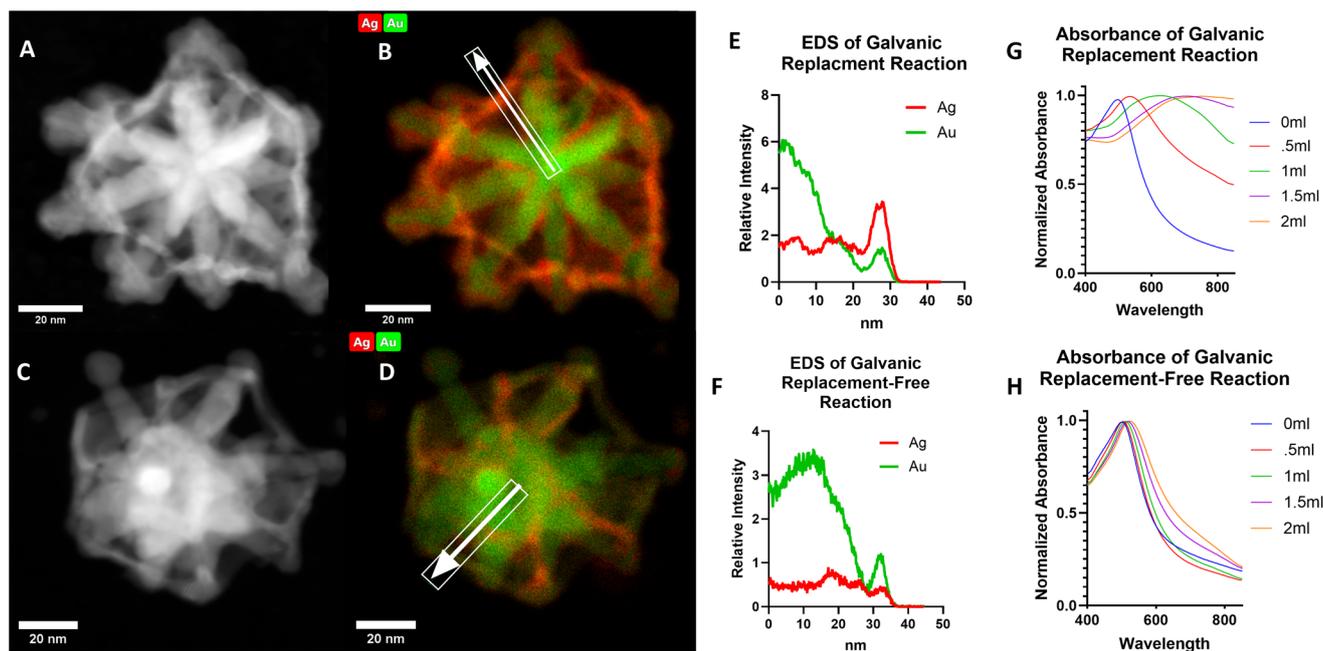
Fig. 2 Comparison of galvanic replacement and galvanic replacement-free synthetic routes to achieve C-GNS. (A) HAADF-STEM image of C-GNS particle prepared *via* galvanic replacement reaction. (B) STEM-EDS image of particle shown in A, ROI for elemental analysis shown in the white box. (C) HAADF-STEM image of C-GNS particle prepared *via* galvanic replacement-free reaction. (D) STEM-EDS image of the particle shown in C, ROI for elemental analysis shown in the white box. (E) Elemental analysis of region shown in B as a function of distance. (F) Elemental analysis of region shown in D as a function of distance. (G) Absorption spectra of nanoparticle solution as a function of gold added for the galvanic replacement reaction. (H) Absorption spectra of nanoparticle solution as a function of gold added for the galvanic replacement-free reaction.

After adding equal quantities of gold chloride solution, the peak absorption value for the C-GNS particles prepared *via* galvanic replacement was red-shifted by 210 nm. In contrast, the peak absorption value for the galvanic-replacement free particle solution red-shifted by 17 nm. Only after peroxide etching of the internal silver layer does the peak absorbance value of the galvanic replacement-free particle shift to the NIR. The novel ionic-surfactant-free C-GNS morphology can be achieved *via* either synthetic route. However, for potential downstream *in vivo* applications, only those prepared *via* the galvanic replacement-free method will be considered due to their significantly lower gold-to-silver alloy ratio. Gold nanoparticles are attractive vehicles for a wide variety of *in vivo* applications, partially because they have the lowest associated toxicity of all metal nanoparticles.[27] In *in vivo* studies, silver nanoparticles have been shown to cause greater ROS production than their gold counterparts.[28] However, in a study examining the biocompatibility of gold, silver, and gold–silver alloy nanoparticles, no significant difference in cell maturation or expansion was observed between gold nanoparticles and 1 : 1 gold–silver alloy particles.[29] Therefore, we have chosen the galvanic replacement-free synthetic route, which results in the lowest amount of gold–silver alloy formation in the shell of the C-GNS.

To examine the effects of C-GNS on cell viability, an MTT cytotoxicity study was performed where MB49 cells were incubated with different concentrations of nanoparticles for 24 hours, shown in Fig. S2B.† Negligible cellular toxicity was observed with C-GNS particles prepared using either galvanic replacement or galvanic replacement-free techniques in the range of 10 μg mL^{-1} to 90 μg mL^{-1}. However, at the highest concentration of nanoparticles tested, 180 μg mL^{-1}, C-GNS particles prepared *via* galvanic replacement were significantly more toxic than the same concentration of particles prepared *via* the galvanic replacement-free method. The low cytotoxicity trends seen for the galvanic replacement-free C-GNS particles are consistent with several studies that examined gold nanoparticle cytotoxicity.[30–34]

After successfully developing a method to create a hollow shell around a GNS, we investigated the SERS reporter loading of the C-GNS. Unsealed C-GNS were washed several times in ethanol to remove surface-bound PVP and to allow access to the etched openings across the shell surface, which are clearly visible in the high-resolution STEM image shown in Fig. S3.† HITC dye was added to the C-GNS ethanol solution and mixed overnight, ensuring maximal dye diffusion. Aliquots of dye-loaded nanoparticle solution were redispersed individually into an aqueous PVP solution and coated with a final layer of gold. The final molar ratio of gold chloride to nanoparticles in solution was 7.5 × 10^5. After the final coating, the particles were washed several times in ethanol and incubated in a 20 μM COOH-PEG$_{5000}$-SH ethanol solution at 50 °C overnight to remove surface-adsorbed PVP and dye completely.

Fig. 3A contains a HAADF-STEM image of sealed C-GNS particles. Nanoparticle tracking analysis results in Fig. S4A† reveal that sealed C-GNS particles in solution are monodis-
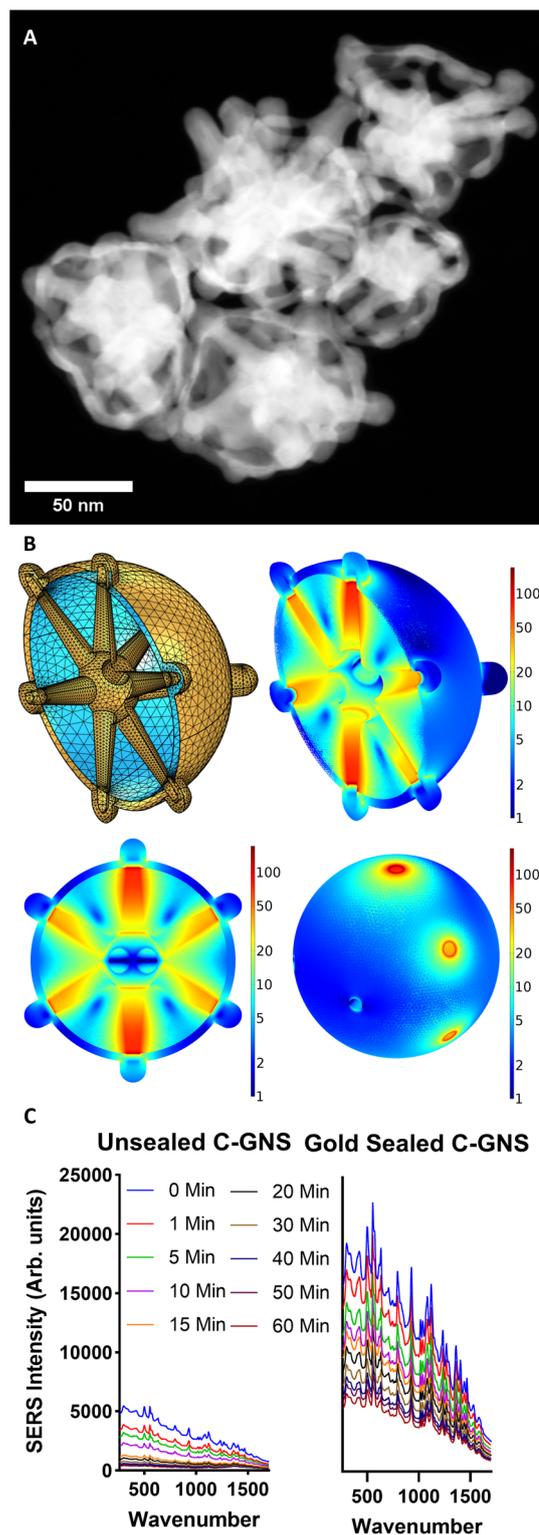
Fig. 3 Investigation of sealed C-GNS particles. (A) HAADF–STEM image of sealed C-GNS particles. (B) COMSOL model and simulations results of sealed C-GNS excited with 785 nm light. (C) SERS intensity of unsealed and sealed C-GNS particles over time in dilute H$_2$O$_2$ solution.

persed, with an average hydrodynamic diameter of 102.2 nm ± 17.8 nm. There is a noticeable increase in both the thickness of the outer shell of the particle and a broadening of exposed branch tips. These morphological changes result in a slightly blue-shifted spectrum, with a peak absorbance value at 730 nm, as seen in ESI Fig. S4B.† The final gold coating step enables the encapsulation of cargo within the shell of the C-GNS and the removal of silver ions deposited on the initial C-GNS shell *via* galvanic replacement, thus further reducing the silver contained within the C-GNS shell. The shell coating thickness of the model shown in supporting Fig. S1B† was increased to 4 nm and simulated with an excitation wavelength of 785 nm to evaluate the theoretical performance of a sealed C-GNS particle. A cross-section of the nanoparticle model is shown in the top left of Fig. 3B. The top right and bottom left of Fig. 3B shows a cross-section of the normalized electric field with the core nanostar removed for clarity. A maximum normalized electric field enhancement $|E|/|E_o|$ value of 171.3 V m^{-1} is generated within the C-GNS shell. The image in the bottom right of Fig. 3B is a perspective view of the normalized electric field only within the inner water domain of the nanoparticle. This region is of greatest interest because it is the dye encapsulation region. The greatest degree of electric field enhancement occurs in a toroidal zone at each branch-shell interface. Therefore, there are as many areas of extremely high field enhancement as GNS branches.

To confirm that the HITC dye was sealed with the C-GNS and not adsorbed onto the particle surface, aliquots of sealed and unsealed C-GNS particles were tested with hydrogen peroxide. First, an aliquot of unsealed C-GNS from the dye-loading solution was centrifuged and resuspended in an aqueous PVP solution so the fluorescence of the unloaded dye would not interfere with subsequent measurements. H_2O_2 was added to sealed and unsealed C-GNS samples, and SERS measurements were recorded over 1 hour. The resulting spectra are shown in Fig. 3C. Before adding H_2O_2, the SERS signal of the uncoated CNS sample was much lower than that of the same concentration of sealed C-GNS particles. The unsealed C-GNS may have lost internally diffused dye during centrifugation before being resuspended, and therefore less dye was present in the highly-enhancing branch-shell interface zones. After adding H_2O_2, the SERS signal intensity of both samples decreased. However, the unsealed samples experienced a near-complete signal loss after 15 minutes of exposure. Additionally, a sample was prepared where dye was sealed within the particles, but the surface-adsorbed dye and PVP were not removed. As shown in Fig. S5,† the fluorescence of the sample decreases rapidly upon adding H_2O_2, and then the SERS signal gradually decreases over 1 hour. This two-step process represents the initial destruction of dye that is not encapsulated within the C-GNS and then the gradual degradation of the particles. Compared to the unsealed sample, the relatively slow signal decay observed in the sealed C-GNS sample is strong evidence of effectively encapsulated cargo.

Finally, we investigated the potential utility of sealed C-GNS as theranostic nanoparticles for *in vivo* detection and photo-

thermal therapy. Particles were first characterized using an agarose gel phantom, shown in ESI Fig. S6.† Fig. 4A shows the total emission of the phantom when excited with 785 nm light. The peak absorption wavelength for this fluorescent dye is 740 nm, therefore while further increasing the SERS signal of these particles *via* resonant Raman scattering, there is also an appreciable fluorescent background.[35] We then used a liquid crystal tunable filter with a 0.75 nm FWHM bandpass to
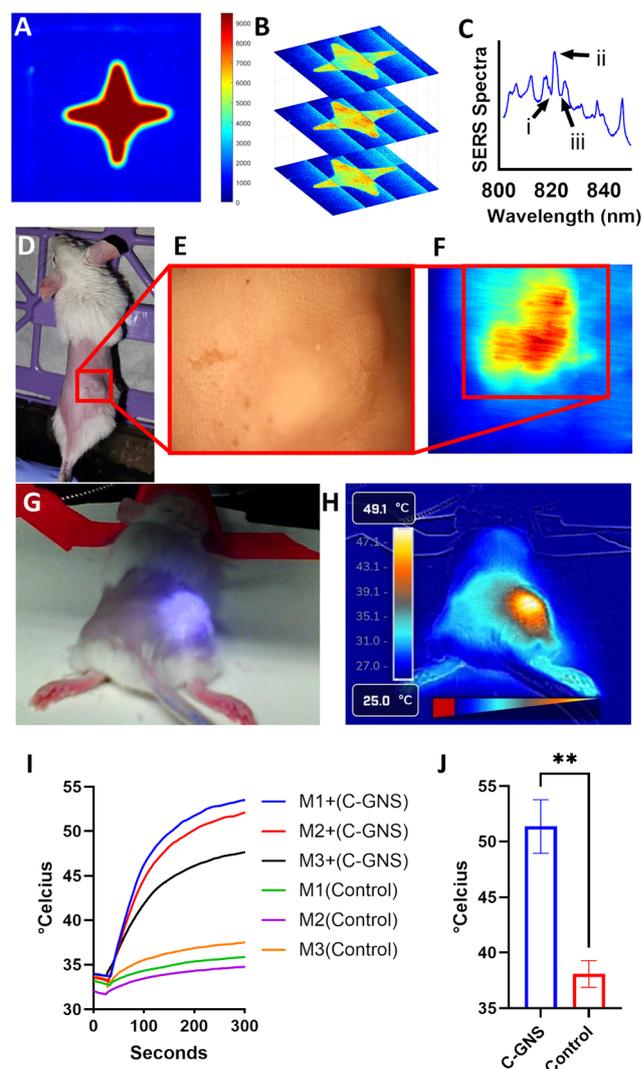
Fig. 4 Potential theranostic application of C-GNS particles. (A) The total emission of an agarose phantom incorporated with C-GNS. (B) Slices from a hyperspectral imaging data cube of a C-GNS phantom at 820, 822, and 824 nm. (C) A reference HITC dye SERS spectra, with annotated points i, ii, and iii corresponding to the bottom, middle and top slices shown in B, respectively. (D) Picture of a mouse 24 hours after retroorbital C-GNS injection, flank tumor within the highlighted region. (E) Brightfield image from SERS microscope of corresponding tumor region. (F) Hyperspectral image of tumor region at 822 nm. (G) Brightfield image of photothermal treatment. (H) Thermal camera image of photothermal treatment. (I) Thermocouple temperature data of tumor interior during photothermal treatment. (J) Highest temperatures observed with a thermal camera during photothermal treatment.

directly image the phantom at 820, 822, and 824 nm respectively. The resulting direct images at these wavelengths are shown in Fig. 4B in ascending order. The reference spectra of HITC dye in C-GNS are shown in Fig. 4C, where the labels i, ii, and iii correspond to the bottom, middle and top slices of Fig. 4B. While there is a significant signal due to the background fluorescence of the dye, there is a noticeable increase in the signal of the center slice in Fig. 4B. Next, we performed a photothermal characterization study of sealed C-GNS particles to assess their utility in therapeutic *in vivo* applications. The temperature of a nanoparticle solution was recorded during exposure to 1064 nm until the solution reached equilibrium and then allowed to cool to room temperature, resulting in the heating curve shown in Fig. S7A.† Using this curve and the method demonstrated by Ayala-Orozco *et al.*,[36] a photothermal conversion efficiency of 86.9% was obtained for the C-GNS sample. Then a one-hour laser cycling study was performed, revealing the robust photothermal stability of the nanoparticle solution, shown in Fig. S7B.† To evaluate the *in vivo* performance of the gold-coated C-GNS, a flank tumor model of murine bladder cancer was established by injecting 2.5×10^5 MB49 cells into female B6 albino mice aged 8–12 weeks. Once the tumor volumes reached 100–200 mm³, 1.5 mg of C-GNS particles were administered *via* retroorbital injection. Fig. 4D shows a mouse 24 hours after nanoparticle injection; the tumor is in the highlighted region. Fig. 4E is a bright field image of the tumor region through the laboratory-built microscope system, and Fig. 4F shows the hyperspectral image of the same area at 822 nm. The high similarity between the bright field and hyperspectral images demonstrates the passive accumulation of C-GNS within the tumor microenvironment.

For an initial photothermal therapy investigation, a total of 6 mice received photothermal treatment with 600 mW cm⁻² at an FDA-approved wavelength of 1064 nm for 10 minutes. Three mice received an injection of 1.5 mg C-GNS, and three were used as controls. The bright field and IR camera images of the photothermal treatment of a mouse that had received C-GNS are shown in Fig. 4G and H. This marked temperature increase is caused by the local increase in NIR absorption generated by the particles and subsequent photon-to-heat conversion. The temperature results of a hypodermic thermocouple placed into the center of the tumor are shown as a function of time for each mouse in Fig. 4I. Measurements began 30 seconds before turning on the laser and continued for another 9 minutes and 30 seconds. At that point, the thermocouple was removed, and an image was taken with the thermal camera at the 10-minute mark of laser treatment. The maximum values of each thermal camera measurement are shown in Fig. 4J. A sharp increase in temperature is observed in thermocouple data upon laser activation for all animals which received C-GNS. The average maximum temperature value measured for the group that received C-GNS was 51.4 °C, whereas the average value for the control group was 38.1 °C. The unit used to evaluate clinical hyperthermia is cumulative effective minutes (CEM) at 43 °C over 90% of the tumor

region, see eqn (S1).† Irreversible tissue damage begins at 10 $CEM_{43}90$.[37] For example, if 90% of the tumor volume were 50 °C for 1 minute, the equivalent $CEM_{43}90$ value would equal 128, far exceeding the threshold to induce cellular damage. The application of these tools demonstrates the potential of C-GNS particles as a novel theranostic platform for sensing and treating solid tumors *via* photothermal therapy. Previous nanoparticle dosing regimens were selected as a starting point for this study to illustrate the theranostic potential of the C-GNS platform effectively; in subsequent work, we intend to determine the lowest effective dose specific to C-GNS. Following this promising proof-of-concept study, we intend to rigorously investigate the loading efficiency of various chemotherapeutic agents, biocompatibility, pharmacokinetics, and biodistribution of C-GNS and integrate C-GNS-mediated photothermal therapy at various wavelengths with more sophisticated *in vivo* thermometry techniques.

Conclusion

Although noble metal nanoparticles have been widely used in photothermal therapy, the development of C-GNS has led to the creation of a novel and versatile nanoplatform with a wide variety of potential biomedical applications. The proposed C-GNS structure has several unique and innovative features which are afforded by the novel morphology of the platform. While various solid-core hollow-shelled particles based primarily on nanospheres exist, our investigation marks the exploration and documentation of a caged system with a nanostar core as the foundation for such a platform. We have pioneered a novel surfactant-free synthesis method, circumventing the need for toxic cetyltrimethylammonium bromide (CTAB), to produce biocompatible star-shaped gold nanoparticles suitable for *in vivo* medical applications.[14] The synergistic combination of a caged outer structure with a nanostar core yields distinctive plasmonic properties and versatile functionalities in potential theranostic applications, as expounded upon in our study. Nanostars, characterized by their numerous sharp branches, evoke a "lightning rod" effect, dramatically enhancing the local electromagnetic field. Among nanoparticles, nanostars exhibit exceptional promise owing to their distinctive tip-enhanced plasmonics properties, which yield intensely enhanced Surface-Enhanced Raman Scattering (SERS) signals for improved detection sensitivity when analytes are adsorbed onto the nanostars. The outer cage structure is meticulously designed to encapsulate the Raman dye and prevent its leakage from the system while retaining the desirable optical properties of nanostars.

In this work, we have synthesized C-GNS particles *via* two synthetic routes to highlight the advantages of the galvanic replacement-free preparation method. FEM simulations of sealed C-GNS particles were utilized to investigate the strong local electric field enhancement generated within the hollow shell of this novel plasmonic nanostructure. We then successfully demonstrated that cargo can be effectively encapsulated

within the C-GNS shell and the C-GNS platform utility for potential *in vivo* theranostic applications including hyperspectral imaging for tumor localization and photothermal therapy for the ablation of solid tumors in a mouse model. This next generation of plasmonic nanoparticle platform technologies offers vastly improved properties for sensing and photothermal treatment of tumors and has the potential to significantly impact the field of nanomedicine.

Conflicts of interest

There are no conflicts to declare.

Acknowledgements

References

1 J. Langer, D. Jimenez de Aberasturi, J. Aizpurua, R. A. Alvarez-Puebla, B. Auguié, J. J. Baumberg, G. C. Bazan, S. E. J. Bell, A. Boisen, A. G. Brolo, J. Choo, D. Cialla-May, V. Deckert, L. Fabris, K. Faulds, F. J. García de Abajo, R. Goodacre, D. Graham, A. J. Haes, C. L. Haynes, C. Huck, T. Itoh, M. Käll, J. Kneipp, N. A. Kotov, H. Kuang, E. C. Le Ru, H. K. Lee, J.-F. Li, X. Y. Ling, S. A. Maier, T. Mayerhöfer, M. Moskovits, K. Murakoshi, J.-M. Nam, S. Nie, Y. Ozaki, I. Pastoriza-Santos, J. Perez-Juste, J. Popp, A. Pucci, S. Reich, B. Ren, G. C. Schatz, T. Shegai, S. Schlücker, L.-L. Tay, K. G. Thomas, Z.-Q. Tian, R. P. Van Duyne, T. Vo-Dinh, Y. Wang, K. A. Willets, C. Xu, H. Xu, Y. Xu, Y. S. Yamamoto, B. Zhao and L. M. Liz-Marzán, *ACS Nano*, 2020, **14**, 28–117.

2 L. Xu, W. Yan, W. Ma, H. Kuang, X. Wu, L. Liu, Y. Zhao, L. Wang and C. Xu, *Adv. Mater.*, 2015, **27**, 1706–1711.

3 D.-P. Yang, X. Liu, C. P. Teng, C. Owh, K. Y. Win, M. Lin, X. J. Loh, Y.-L. Wu, Z. Li and E. Ye, *Nanoscale*, 2017, **9**, 15753–15759.

4 P. S. Kumar, I. Pastoriza-Santos, B. Rodríguez-González, F. Javier García de Abajo and L. M. Liz-Marzán, *Nanotechnology*, 2008, **19**, 015606.

5 T. K. Sau and C. J. Murphy, *J. Am. Chem. Soc.*, 2004, **126**, 8648–8649.

6 B. L. Sanchez-Gaytan, P. Swanglap, T. J. Lamkin, R. J. Hickey, Z. Fakhraai, S. Link and S.-J. Park, *J. Phys. Chem. C*, 2012, **116**, 10318–10324.

7 S. Atta, M. Beetz and L. Fabris, *Nanoscale*, 2019, **11**, 2946–2958.

8 C. Heck, Y. Kanehira, J. Kneipp and I. Bald, *Angew. Chem., Int. Ed.*, 2018, **57**, 7444–7447.

9 D. Dong, Q. Shi, D. Sikdar, Y. Zhao, Y. Liu, R. Fu, M. Premaratne and W. Cheng, *Nanoscale Horiz.*, 2019, **4**, 940–946.

10 T. Vo-Dinh, *TrAC, Trends Anal. Chem.*, 1998, **17**, 557–582.

11 T. Vo-Dinh, M. Y. K. Hiromoto, G. M. Begun and R. L. Moody, *Anal. Chem.*, 1984, **56**, 1667–1670.

12 M. Volkan, D. L. Stokes and T. Vo-Dinh, *Appl. Spectrosc.*, 2000, **54**, 1842–1848.

13 F. Yan, M. B. Wabuyele, G. D. Griffin, A. A. Vass and V.-D. Tuan, *IEEE Sens. J.*, 2005, **5**, 665–670.

14 H. Yuan, C. G. Khoury, H. Hwang, C. M. Wilson, G. A. Grant and T. Vo-Dinh, *Nanotechnology*, 2012, **23**, 075102.

15 Y. Liu, P. Maccarini, G. M. Palmer, W. Etienne, Y. Zhao, C. T. Lee, X. Ma, B. A. Inman and T. Vo-Dinh, *Sci. Rep.*, 2017, **7**, 8606.

16 A. M. Fales, H. Yuan and T. Vo-Dinh, *J. Phys. Chem. C*, 2014, **118**, 3708–3715.

17 S. Atta and T. Vo-Dinh, *Anal. Chim. Acta*, 2023, **1251**, 340956.

18 A. J. Canning, X. Chen, J. Q. Li, W. R. Jeck, H.-N. Wang and T. Vo-Dinh, *Biosens. Bioelectron.*, 2023, **220**, 114855.

19 Y. Yang, J. Liu, Z. W. Fu and D. Qin, *J. Am. Chem. Soc.*, 2014, **136**, 8153–8156.

20 A. S. De Silva Indrasekara, S. F. Johnson, R. A. Odion and T. Vo-Dinh, *ACS Omega*, 2018, **3**, 2202–2210.

21 X. Xia, Y. Wang, A. Ruditskiy and Y. Xia, *Adv. Mater.*, 2013, **25**, 6313–6333.

22 X. Lu, L. Au, J. McLellan, Z.-Y. Li, M. Marquez and Y. Xia, *Nano Lett.*, 2007, **7**, 1764–1769.

23 S. Atta, T. V. Tsoulos and L. Fabris, *J. Phys. Chem. C*, 2016, **120**, 20749–20758.

24 Y. Liu, P. Chongsathidkiet, B. M. Crawford, R. Odion, C. A. Dechant, H. R. Kemeny, X. Cui, P. F. Maccarini, C. D. Lascola, P. E. Fecci and T. Vo-Dinh, *Immunotherapy*, 2019, **11**, 1293–1302.

25 Y. Liu, H. Yuan, A. M. Fales, J. K. Register and T. Vo-Dinh, *Front. Chem.*, 2015, **3**, 51.

26 V. P. Chauhan, T. Stylianopoulos, J. D. Martin, Z. Popović, O. Chen, W. S. Kamoun, M. G. Bawendi, D. Fukumura and R. K. Jain, *Nat. Nanotechnol.*, 2012, **7**, 383–388.

27 M. Kus-Liśkiewicz, P. Fickers and I. Ben Tahar, *Int. J. Mol. Sci.*, 2021, **22**(20), 10952.

28 A. Ávalos, A. I. Haza, D. Mateo and P. Morales, *Toxicol. Mech. Methods*, 2015, **25**, 287–295.

29 D. Tiedemann, U. Taylor, C. Rehbock, J. Jakobi, S. Klein, W. A. Kues, S. Barcikowski and D. Rath, *Analyst*, 2014, **139**, 931–942.

30 P. Manivasagan and J. Oh, *Mar. Drugs*, 2015, **13**, 6818–6837.

31 Y. J. Lee, E.-Y. Ahn and Y. Park, *Nanoscale Res. Lett.*, 2019, **14**, 129.

32 G. Vales, S. Suhonen, K. M. Siivola, K. M. Savolainen, J. Catalán and H. Norppa, *Nanomaterials*, 2020, **10**, 271.

33 M. N. Bin-Jumah, M. Al-Abdan, G. Al-Basher and S. Alarifi, *Dose-Response*, 2020, **18**, 1559325820912154.

34 R. Rudolf, B. Friedrich, S. Stopić, I. Anžel, S. Tomić and M. Čolić, *J. Biomater. Appl.*, 2012, **26**, 595–612.

35 H. Yuan, Y. Liu, A. M. Fales, Y. L. Li, J. Liu and T. Vo-Dinh, *Anal. Chem.*, 2013, **85**, 208–212.

36 C. Ayala-Orozco, C. Urban, M. W. Knight, A. S. Urban, O. Neumann, S. W. Bishnoi, S. Mukherjee, A. M. Goodman, H. Charron, T. Mitchell, M. Shea, R. Roy, S. Nanda, R. Schiff, N. J. Halas and A. Joshi, *ACS Nano*, 2014, **8**, 6372–6381.

37 G. C. van Rhoon, T. Samaras, P. S. Yarmolenko, M. W. Dewhirst, E. Neufeld and N. Kuster, *Eur. Radiol.*, 2013, **23**, 2215–2227.